Chemical Science

ROYAL SOCIETY OF CHEMISTRY

EDGE ARTICLE

View Article Online
View Journal | View Issue

Cite this: *Chem. Sci.*, 2026, **17**, 1029

All publication charges for this article have been paid for by the Royal Society of Chemistry

Surface dynamic engineering of discontinuous cobalt dopants on copper sulfide for enhanced electrosynthesis of hydrogen peroxide

Changhui Sun,[a] Chaoqun Ma,[b] Xuyun Guo,[cd] Yingjun Ma,[a] Qiying Yang,[a] Liangyu Gong, *[a] Ye Zhu,[c] Valeria Nicolosi [d] and Jie Wang *[a]

Received 13th August 2025
Accepted 30th October 2025

DOI: 10.1039/d5sc06179b

rsc.li/chemical-science

Electrochemical synthesis of hydrogen peroxide (H_2O_2) represents a sustainable, economical, and energy-efficient approach but faces challenges due to sluggish and complicated dynamics at the solid/liquid/gas interface. This study leverages theoretical insights from CuS surface microenvironments, demonstrating that cobalt doping and edge defects on CuS can thermodynamically favor the 2-electron oxygen reduction reaction ($2e^-$-ORR) pathway for H_2O_2 production. To validate theoretical predictions, we synthesized a catalyst featuring interleaved hexagonal lamellar copper sulfide with discontinuous cobalt dopants at the edges and complementary defects (Co-CuS_{ED}). This design optimizes the microelectronic structure at the electrocatalytic interface, enhancing the $2e^-$-ORR pathway over the 4-electron pathway. The optimized Co-CuS_{ED} achieves a high H_2O_2 production rate of 1.10 mol g_{cat}^{-1} h^{-1}. Using this catalyst in a dual cathode system for *in situ* H_2O_2 generation results in rapid degradation of organic dyes, reaching 92% efficiency within 20 minutes. This work presents an environmentally friendly, cost-effective, and efficient strategy for H_2O_2 electrosynthesis, with strong potential for wastewater remediation.

Introduction

The acceleration of industrialization has significantly boosted productivity, but it has also led to serious environmental challenges due to the discharge of industrial and agricultural wastewater.[1] Once released into the environment, they will inevitably cause severe damage to ecosystems.[2] Therefore, it is crucial to remove the pollutants in time. Hydrogen peroxide (H_2O_2) is a versatile oxidant and an emerging sustainable energy carrier, efficient in fields of wastewater treatment.[3,4] To date, the predominant large-scale production method, the anthraquinone process, remains restricted by high operational costs, substantial energy consumption, and significant environmental and safety concerns.[5,6] Alternatively, *in situ* generation of H_2O_2 *via* electrocatalytic processes has shown promise in wastewater treatment,[7–9] enabling the immediate degradation of pollutants upon production. It not only enhances treatment efficiency but also eliminates the need for centralized H_2O_2 production, transportation, and repeated chemical dosing, thereby simplifying the overall process.[10,11] However, the electrochemical two-electron oxygen reduction reaction ($2e^-$-ORR),[12,13] which utilizes O_2 and H_2O as precursors, suffers from sluggish kinetics and the competing four-electron ($4e^-$) ORR pathway that act as obstacles for high efficiency H_2O_2 generation.[14–16]

To address these challenges, designing electrocatalysts with superior activity and selectivity for the $2e^-$-ORR is imperative.[17–19] A diverse array of catalysts, including noble metals, transition metal compounds, and metal-free alternatives, have been explored.[20–22] Although noble metals have proved to exhibit excellent catalytic performance, their high cost, scarcity, and toxicity severely limit scalability.[23,24] Consequently, non-precious metal catalysts, particularly transition metal sulfides (TMS), have attracted significant attention due to their cost-effectiveness and superior electrical conductivity compared to most transition metal oxides and hydroxides. These advantages stem from the differences in electronegativity and atomic radius between oxygen and sulfur atoms, which influence charge distribution and bonding characteristics in the lattice.[25] Nonetheless, pristine TMS often suffer from limited active site density and poor electrochemical stability, constraining their catalytic performance. To address these limitations, both intrinsic and extrinsic activities can be enhanced through electronic structure modulation *via* interface engineering and defect engineering.[26,27] For example, Viswanathan and co-workers revealed, from a surface reconstruction perspective, that the ORR catalytic activity of nickel sulfides is primarily governed by the Ni–S coordination number at surface-

[a]*College of Chemistry and Pharmaceutical Sciences, Qingdao Agricultural University, Qingdao 266109, China. E-mail: wangjie@qau.edu.cn; lygong@qau.edu.cn*

[b]*School of Materials Science and Engineering, University of Science and Technology Beijing, Beijing 100083, China*

[c]*Department of Applied Physics, Research Institute for Smart Energy, The Hong Kong Polytechnic University, Hung Hom, Kowloon, Hong Kong, China*

[d]*School of Chemistry, Centre for Research on Adaptive Nanostructures and Nanodevices (CRANN) and Advanced Materials Bio-Engineering Research Centre (AMBER), Trinity College Dublin, Dublin D02PN40, Ireland*

exposed sites within the reconstructed amorphous phases.[28] Mai and co-workers demonstrated that interfacial coupling and sulfur vacancies synergistically modulate the electronic structure of a copper–nickel sulfide heterojunction catalyst, effectively enhancing the adsorption behavior of oxygen intermediate species and significantly lowering the energy barrier for the ORR.[29] As a member of TMS, copper sulfide (CuS), a p-type semiconductor, possesses a distinctive bandgap structure that facilitates structural modifications.[30,31] Despite this, the inherent limitations in optimizing the electronic structure of CuS alone hinder significant improvements in the adsorption free energy of *OOH, which is recognized as the rate-determining step in the 2e$^-$-ORR process. As a result, effectively enhancing the electronic structure of CuS to optimize *OOH adsorption remains a significant challenge. Heteroatom doping has emerged as a revolutionary approach to fine-tuning the electronic properties of catalysts, thereby significantly boosting their catalytic activity.[32–34] By precisely regulating the electronic structure and exposing a wealth of active sites, this method offers unprecedented control over catalytic performance. Notably, cobalt (Co) stands out due to its distinctive d-orbital configuration, which enables it to dramatically influence the electron density of host materials, thereby modulating the charge state and chemical reactivity of surface atoms.[35] However, conventional methods that rely on the random dispersion of cobalt dopants within the host catalyst fail to fully unlock its catalytic potential, resulting in inefficient utilization of active sites. The stochastic distribution of dopants leads to spatial and electronic heterogeneity, which is particularly detrimental in surface-sensitive processes such as the 2e$^-$-ORR, critical for the electrosynthesis of H_2O_2. On the other hand, a dense distribution of heteroatom dopants on the catalyst surface can limit the interaction between the host CuS and O_2, reducing its effectiveness for the 2e$^-$-ORR. To address these challenges, it is significant to explore new strategies to synthesize CuS with highly electrochemically active interfaces with a uniform yet discontinuous distribution of Co dopants at the edges of the materials, leveraging edge effects to maximize exposure and enhance intrinsic catalytic activities of the 2e$^-$-ORR.

In this study, we leverage theoretical insights from CuS surface microenvironments, demonstrating that cobalt doping and edge defects on CuS can thermodynamically favor the 2e$^-$-ORR pathway for H_2O_2 production. To validate theoretical predictions, we constructed a novel surface Co-doped CuS (Co-CuS) catalyst with hexagonal lamellar microsphere architecture and engineered edge defects (Co-CuS$_{ED}$) for the target to enhance 2e$^-$-ORR performance. The discontinuous surface distribution of Co dopants at the edges, coupled with a complementary arrangement of defects, can be precisely controlled by tuning the H_2O_2 concentrations during material synthesis. These edge defects effectively optimize the electronic interaction from the surface to the inner bulk CuS framework. The Co-CuS$_{ED}$ catalyst induces favorable charge redistribution, yielding optimal *OOH adsorption and significantly reducing the energy barrier for the 2e$^-$-ORR compared to pristine CuS and uniformly doped Co-CuS. Synchrotron radiation X-ray absorption near-edge structure (XANES) spectroscopy corroborates these findings, demonstrating altered Cu–S bond energy and Cu oxidation states induced by Co doping and defect engineering. The optimized Co-CuS$_{ED}$ catalyst exhibits exceptional selectivity for H_2O_2 production. Importantly, its robust performance extends to natural air diffusion conditions. Practical application is demonstrated through the *in situ* degradation of organic dyes like Rhodamine B (RhB) using dual cathode technology, achieving high degradation rates and recyclability. This work provides crucial insights into the strategic design of heteroatom-doped, defect-modified electrocatalysts, paving the way for scalable, sustainable H_2O_2 production.

Results and discussion

Given the critical role of the ORR at the catalyst interface, a dense distribution of heterogeneous Co dopants on the surface might hinder effective interaction with the host CuS. In consideration, introducing edge defects to achieve a discontinuous distribution of Co dopants is proposed as a strategy to optimize the electronic structure of CuS, thereby enhancing the thermodynamic favorability for the 2e$^-$-ORR pathway. To investigate this hypothesis, Density Functional Theory (DFT) calculations were performed. These calculations focused on elucidating the fundamental mechanisms by which Co doping, in conjunction with edge defect engineering facilitated by the addition of H_2O_2 during synthesis, influences ORR performance. Three theoretical models representing different stabilized adsorption configurations of ORR intermediates (*OOH, *O, *OH) related to CuS, Co-CuS, and Co-CuS$_{ED}$ were established and optimized (Fig. 1a and S1). After calculation, volcano plots were constructed to illustrate the catalytic tendency of different catalysts (Fig. 1b). The plots show that the free energy change (ΔG) of ΔG_{*OH} primarily determines the 4e$^-$-ORR, while ΔG_{*OOH} controls H_2O_2 production *via* the 2e$^-$-ORR. Previous studies have identified an approximate linear relationship between ΔG_{*OH} and ΔG_{*OOH}.[36] Strong adsorption of *OOH or *OH corresponds to the left side of the volcano plot, indicating a preference for breaking the O–O bond and proceeding *via* the 4e$^-$-ORR pathway. In contrast, weak adsorption corresponds to the right slope. Notably, the ΔG_{*OOH} of Co-CuS$_{ED}$ is 4.15 eV, close to the optimal *OOH adsorption energy of 4.22 eV (corresponding to a limiting potential of 0.70 V). This value is comparable to those of high-performance catalysts, such as Pd, Pt, Au/Pt, and Hg/Pt.[37]

To further study the evolution of physical properties resulting from Co doping and edge defects, partial density of states (PDOS) for CuS, Co-CuS, and Co-CuS$_{ED}$ were calculated, as shown in Fig. 1c. The d-band centers for host Cu in CuS, Co-CuS, and Co-CuS$_{ED}$ were determined to be −2.11 eV, −2.09 eV, and −2.04 eV, respectively, of which the d-band center of Co-CuS$_{ED}$ is much closer to the Fermi energy level, beneficial to facilitate the adsorption of intermediates, thereby enhancing the catalytic performance. Fig. 1d presents the charge density difference maps for *OOH adsorption on CuS, Co-CuS, and Co-CuS$_{ED}$, revealing that the number of electrons transferred to *OOH is 1.331*e*, 1.298*e*, and 1.271*e*, respectively. Co-CuS$_{ED}$

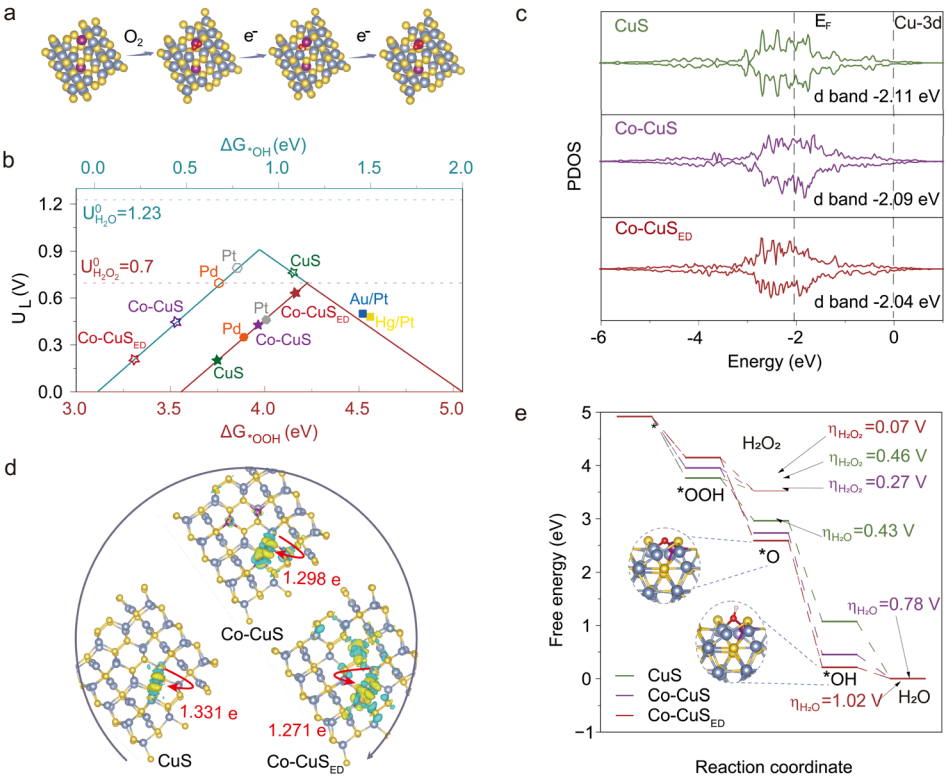

Fig. 1 (a) Schematic diagrams of the theoretical model of Co-CuS_{ED} and the corresponding ORR pathway. (b) Volcano plot depicting the free energy change of reaction intermediates (ΔG_{*OH} and ΔG_{*OOH}) of different Co–Cu–S coordination structures. The data for Pt, Pd, Hg/Pt, and Au/Pt were obtained from ref. 37. (c) PDOS of CuS, Co-CuS and Co-CuS_{ED}. (d) The charge density difference maps of CuS, Co-CuS and Co-CuS_{ED} with adsorption of *OOH (isosurface value = 0.002 e Å^{-3}). (e) Free energy diagram of the ORR for CuS, Co-CuS and Co-CuS_{ED}.

exhibits minimal electron transfer, leading to the weakest *OOH adsorption and the lowest adsorption energy. This suggests that fewer transferred electrons and lower adsorption energy promote *OOH desorption and H_2O_2 formation, reduce the reaction energy barrier, and significantly improve catalytic performance. Fig. 1e illustrates the typical 2e$^-$-ORR process, where O_2 binds to the catalyst surface, followed by the formation of *OOH, and ultimately H_2O_2. Specifically, thermodynamic calculations (eqn (S1)) reveal that the overpotential (η) for the 2e$^-$-ORR on Co-CuS_{ED} is 0.07 V, significantly lower than those for Co-CuS ($\eta = 0.27$ V) and CuS ($\eta = 0.46$ V). In contrast, for the 4e$^-$-ORR pathway leading to H_2O formation, the thermodynamic overpotentials increase in the order: CuS ($\eta = 0.43$ V) < Co-CuS ($\eta = 0.78$ V) < Co-CuS_{ED} ($\eta = 1.02$ V). These results indicate that Co-CuS_{ED} favors the 2e$^-$-ORR pathway, whereas CuS prefers the 4e$^-$-ORR pathway.

According to the theoretical calculations, Co-CuS with interleaved lamellar structures was synthesized *via* a simple solvothermal process followed by post-annealing in a mixed Ar/H_2 atmosphere (Fig. 2a). The lamellar features regular hexagonal shapes with uniform surface cobalt enrichment. By varying the concentration of H_2O_2 during the solvothermal process, the Co dopants and edge defects on the surface can be precisely tuned to optimize the electronic structure. Fig. 2b shows the XRD patterns of the different catalysts. The Cu-containing catalysts display diffraction peaks consistent with the characteristic hexagonal structure of CuS (PDF#06-0464). In contrast, the copper-free catalyst synthesized *via* the same method demonstrates a $CoSO_x$ phase (PDF#54-1124). Notably, no peaks associated with Co-containing phases are observed, likely due to the low concentration or poor crystallization of cobalt in the products.

Raman spectra were performed to probe the surface structure (Fig. 2c). For pure CuS, a weak peak at ~467.0 cm^{-1} is observed, corresponding to the characteristic stretching vibration mode (A_{1g} symmetry) of the S–S bond in CuS. After Co doping, the S–S bond at ~467 cm^{-1} in Co-CuS is further attenuated, and a new peak at ~656.0 cm^{-1} appears, likely corresponding to the E_g mode of Co. Remarkably, in the Co-CuS_{ED} sample, the S–S bond at ~467 cm^{-1} becomes sharper, and a weak peak at ~262 cm^{-1} associated with the stretching vibration of covalent S–S bonds emerges. This is mainly attributed to the partial destruction of the uniform distribution of cobalt species on the surface due to the introduction of H_2O_2 during synthesis, leading to increased exposure of inner CuS.[38] It is hypothesized that H_2O_2 acts as a structure-regulating agent, modulating the interaction between Co dopants and CuS. Core-level XPS analysis was carried out to further investigate the chemical state of the surface species. The survey XPS spectrum (Fig. S2) confirms the presence of Co, Cu, and S, with specific atomic concentrations detailed in Table S1. The high-resolution Co 2p spectrum (Fig. 2d), fitted using a Gaussian function, shows two spin–orbit peaks and two satellite peaks. For Co-CuS_{ED}, the prominent peaks at 781.0 eV and 796.0 eV

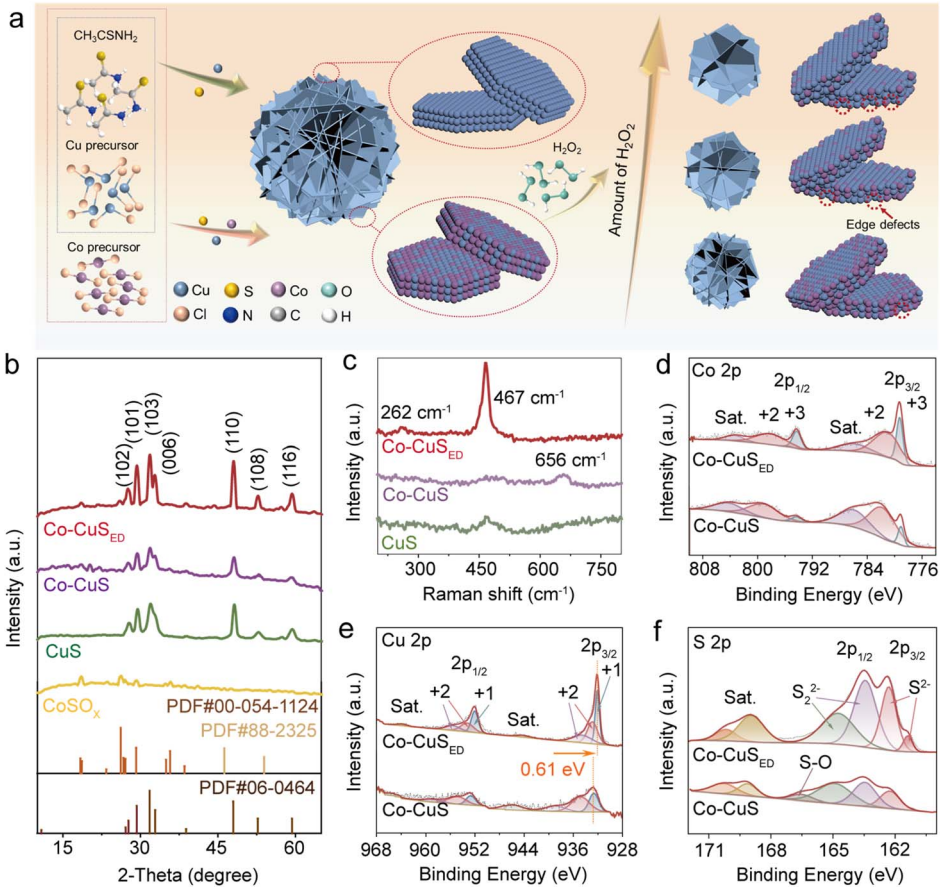

Fig. 2 (a) Schematic illustration of the construction of Co-CuS-based catalysts; (b) XRD patterns of mono-metal sulfides and Co-CuS based catalysts; (c) Raman spectra of CuS, Co-CuS and Co-CuS_{ED}; high-resolution XPS spectra of (d) Co2p, (e) Cu 2p, and (f) S 2p of Co-CuS and Co-CuS_{ED}.

correspond to Co 2p3/2 and Co 2p1/2, respectively. The peaks at 779.1 and 794.5 eV are associated with Co^{3+}, while those at 781.6 eV and 798.6 eV correspond to Co^{2+}. The Cu 2p spectrum (Fig. 2e) reveals peaks at 932.1 eV and 952.1 eV, attributed to Cu^{+}, while the peaks at 933.1, 934.6, 953.4, and 955.0 eV indicates the presence of Cu^{2+}. Compared to Co-CuS, Co-CuS_{ED} shows a clear shift to lower binding energy (0.61 eV), suggesting a conversion from Cu^{2+} to Cu^{+} at the surface after introducing Co dopants and edge defects. The fitted S 2p XPS spectrum (Fig. 2f) shows peaks at 161.4 eV and 162.4 eV, corresponding to the S^{2-} valence state, while peaks at 163.3 eV and 164.3 eV represent bridging S_2^{2-} species in covellite.[39] For Co-CuS_{ED}, the S^{2-} peak appears at 161.4 eV, which is absent in Co-CuS. This shift is likely due to Co reduction, leading to the splitting of S^{2-} ions and the formation of Cu–S and Co–S bonds. Additionally, the disappearance of the S–O bond peak suggests a trend toward the increased formation of Cu–S bonds.[40] The slight shift of the S 2p spectrum to higher binding energies in Co-CuS_{ED}, coupled with the negative shift in Cu 2p, further supports the electronic interactions between Co and CuS after introducing edge defects.

The microstructure of the catalysts was studied using transmission electron microscopy (TEM) techniques. Back-scattered electron scanning TEM (BSE-STEM) images (Fig. 3a and b) of Co-CuS and Co-CuS_{ED} revealed thin lamellar structures (~50 nm in thickness) interleaved together. At higher magnification, the high-angle annular dark-field STEM (HAADF-STEM) image of Co-CuS_{ED} showed regular hexagonal lamellar structures with a side length of approximately 2 μm (Fig. 3c). This morphology provides a higher specific surface area, which is beneficial to increase the electrochemical active area, benefiting the enhancement of oxygen reduction reaction (ORR) activities. High-resolution TEM (HRTEM) images of the hexagonal lamellar for Co-CuS revealed a single-crystal structure (Fig. 3d), with staggered lattice fringes and an intersection angle of 60°. The interplanar spacings of 1.90, 1.90 and 1.90 Å, correspond to the (110), $(\bar{2}10)$ and $(1\bar{2}0)$ planes of CuS. The selected area electron diffraction (SAED) pattern of a single lamella (inset in Fig. 3d) aligns with these HRTEM observations. In comparison, the HRTEM image of Co-CuS_{ED} (Fig. 3e) shows a similar crystal structure, but with distinct edge defects (marked with red arrows), indicating successful creation of edge defects at the lamellar surface through the introduction of H_2O_2 during synthesis. STEM image (Fig. 3f) and corresponding electron energy loss spectroscopy (EELS) maps of Co-CuS showed a Co distribution concentrated at the edges, with uniform distribution of Cu and S. The Co L-edge and Cu L-edge EELS spectra (red arrows) further confirm this distribution from

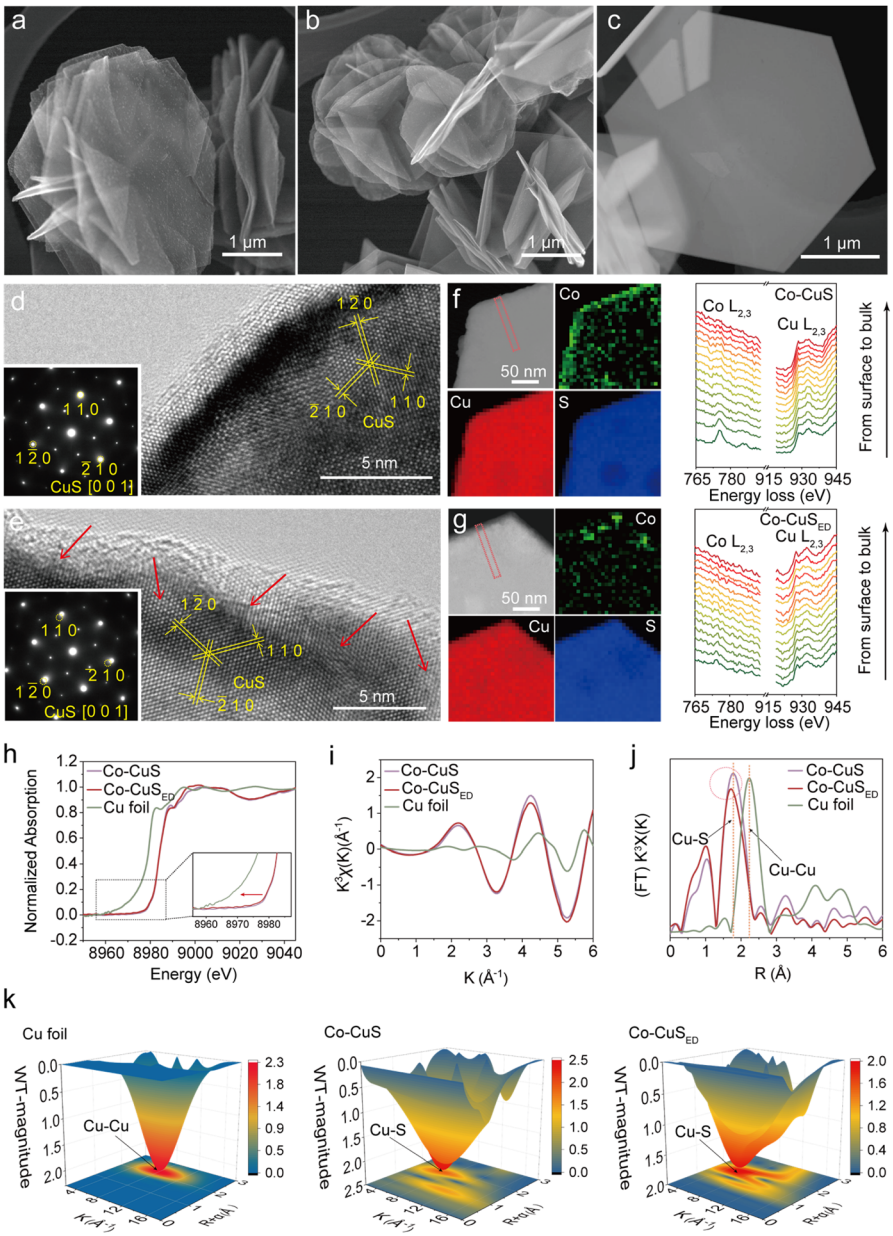

Fig. 3 BSE-STEM images of Co-CuS (a) and Co-CuS_{ED} (b); (c) HAADF-STEM image of a Co-CuS_{ED} lamellar; (d) HRTEM image of Co-CuS and SAED pattern (inset); (e) HRTEM image of Co-CuS_{ED} and SAED pattern (inset); (f) HAADF-STEM image of Co-CuS with EELS elemental maps and corresponding spectra of Co L-edge along the red rectangle direction; (g) HAADF-STEM image of Co-CuS_{ED} with EELS elemental maps and corresponding spectra of Co L-edge along the red rectangle direction; Cu K-edge XANES spectra (h), corresponding FT-EXAFS spectra (i), and corresponding Cu K-edge EXAFS spectra (j) of Co-CuS, Co-CuS_{ED} and standard sample (Cu foil); (k) 3D FT Cu K-edge EXAFS spectra of the standard sample (Cu foil), Co-CuS and Co-CuS_{ED}.

the surface to the bulk. In contrast, Co-CuS_{ED} exhibited a discontinuous Co distribution concentrated at the lamellar edges (Fig. 3g), while Cu and S remained uniformly distributed, consistent with theoretical models established in Fig. 1. A comparison of the Cu L-edge EELS spectra reveals a higher proportion of Cu^{+} in Co-CuS_{ED} compared to Co-CuS.[41] The Co and Cu species showed negligible changes before and after the introduction of edge defects. These nanoscale observations align with the results from Raman and XPS characterization studies (Fig. 2c–e). To further elucidate the evolution of the electronic structure, synchrotron radiation spectroscopy was employed. As shown in Fig. 3h, the Cu K-edge spectra of Co-CuS_{ED} exhibit a slight shift to lower energies compared to Co-CuS, indicating a decrease in the valence of Cu^{2+} due to the introduction of edge defects. Extended X-ray absorption fine structure (EXAFS) spectra (Fig. 3i and j), derived from the Cu K-edge, show similar oscillation patterns in the low-wavenumber range for both Co-CuS and Co-CuS_{ED}, suggesting similar coordination environments. Both samples display a major FT-EXAFS peak at 1.81 Å (Fig. 3j), corresponding to the Cu–S bond.[42]

However, the Co-CuS_{ED} sample exhibits a noticeable left shift and decreased intensity, suggesting shorter bond lengths, enhanced bond strength, and a smaller coordination number. To uncover high-resolution features simultaneously in *K*-space and *R*-space, wavelet transform (WT) analysis was applied to the EXAFS spectral signal, generating a three-dimensional representation (Fig. 3k). Due to the scattering effect of the Cu–S bond, the WT contour plot of Co-CuS_{ED} shows a maximum peak at 8.93 $Å^{-1}$, higher than the 6.86 $Å^{-1}$ peak for Co-CuS.[43] This further verifies that both Co-CuS and Co-CuS_{ED} share the same coordination environment, with Co-CuS_{ED} exhibiting enhanced bonding characteristics.[44]

The evolution of Co-CuS with varying amounts of H_2O_2 during the synthesis process was investigated. As shown in the XRD patterns (Fig. S3), increasing the amount of H_2O_2 not only maintained the CuS phase but also significantly enhanced its crystallinity, demonstrating the structural reinforcing effect of H_2O_2. Inductively coupled plasma optical emission spectrometry (ICP-OES) analysis of catalysts revealed a gradual decrease in cobalt content with increasing H_2O_2 (Table S2). The atomic percentage of Co in Co-CuS catalysts was significantly lower than that of Cu, confirming successful Co-doping. These compositional trends were further verified by XPS surface surveys (Fig. S4 and Table S1). Notably, the higher bulk Cu content detected by ICP-OES *versus* surface-sensitive XPS suggests that Cu is predominantly distributed in the catalyst core, while Co is enriched at the surface. High-resolution XPS spectra of Co 2p, Cu 2p, and S 2p (Fig. S5) showed minimal changes in the valence states of Co and Cu with increasing H_2O_2 concentration. However, upon the addition of 2.0 mL of H_2O_2, no detectable high-resolution Co 2p spectra were observed, suggesting that the Cu species on the catalyst surface had become fully occupied. Additionally, a noticeable shift toward lower binding energy was observed in the high-resolution S 2p XPS spectra, indicating enhanced interaction between Cu and S, further supporting the improved CuS bonding. The morphology evolution associated with increasing volume of H_2O_2 during synthesis was characterized *via* scanning electron microscopy (SEM). Specifically, Co-CuS synthesized with 0.5 mL of H_2O_2 exhibits two distinct morphologies (Fig. S6): microspheres and microspheres interwoven by the nanosheet-like thin lamellar structures. When the H_2O_2 volume is increased to 1.0 mL, the morphology becomes more uniform, predominantly consisting of thin lamellar structures interwoven with microspheres. Further increasing the H_2O_2 volume to 1.5 mL and 2.0 mL results in an even larger sheet size and loose interweaving of nanosheets. To precisely investigate the control of defect concentration through H_2O_2 dosage, electron paramagnetic resonance (EPR) spectroscopy was performed. As shown in Fig. S7, Co-CuS synthesized without H_2O_2 exhibits a negligible signal at $g = 2.004$, indicative of a low defect density. In contrast, a distinct EPR signal emerges when H_2O_2 is introduced during synthesis, and its intensity increases progressively with higher H_2O_2 concentrations. This trend demonstrates the precise tunability of defect concentration by modulating the amount of H_2O_2 used in the synthesis. Combined with the TEM results, these findings suggest that the introduction of varying amounts of H_2O_2 allows for precise control over cobalt content and the creation of edge defects on the surface.

The ORR performance of the catalysts was evaluated using a three-electrode configuration. As shown in Fig. 4a, the oxygen reduction polarization curves obtained with a rotating ring-disc electrode (RRDE) revealed a significantly higher ring current density for Co-CuS_{ED} compared to Co-CuS, CuS, and $CoSO_x$. Specifically, Co-CuS_{ED} exhibited a high Faradaic efficiency (FE) of 60% (Fig. 4b) and H_2O_2 production selectivity of 78%, outperforming the other catalysts (Fig. 4c). Additionally, as the amount of H_2O_2 increased, the ring current decreased (Fig. S8). The corresponding H_2O_2 selectivity and FE initially increased when adding 0.5 to 1.0 mL of H_2O_2, but decreased with higher volumes (1.5 to 2.0 mL, Fig. S9). This trend indicates that the $2e^-$-ORR activity of Co-CuS_{ED} is primarily regulated by the amount of H_2O_2 introduced during the synthesis, which controls the electrocatalytic performance by modulating the concentration of cobalt dopants and edge defects. As shown in Fig. 4d, the electron transfer number (*n*) for Co-CuS_{ED}, measured over a wide potential range of 0.10 to 0.60 V, is calculated to be 2.4 (eqn (S2)–(S4)), which is close to the ideal $2e^-$-ORR process. In contrast, Co-CuS, CuS, and $CoSO_x$ displayed higher *n* values. Notably, Co-CuS_{ED} synthesized with 1.0 mL of H_2O_2 exhibited the smallest *n* value compared to those prepared with 0.5, 1.5, and 2.0 mL of H_2O_2, confirming the excellent two-electron selectivity of Co-CuS_{ED} when synthesized with the optimal H_2O_2 concentration (Fig. S9). To further validate the electron transfer number, polarization curves at different rotational speeds were analyzed, and corresponding K–L plots (Fig. S10) were fitted. Using the Levich equation (eqn (S5) and (S6)), the electron transfer numbers for Co-CuS_{ED} were calculated to range from 2.47 to 2.58 at the potential range between 0.20 and 0.40 V, consistent with the RRDE results. Tafel plots derived from the disc polarization curves in Fig. 4a and S11 are presented in Fig. 4e and S12, in which Co-CuS_{ED} exhibits the lowest slope value (73.18 mV dec^{-1}), indicating a mixed Heyrovsky–Volmer mechanism and enhanced reaction kinetics for the $2e^-$-ORR. A radar chart (Fig. 4g) comprehensively compares the electrochemical properties of CuS, Co-CuS, and Co-CuS_{ED}, in which Co-CuS_{ED} showed optimal performance across all five parameters, reflecting superior reaction activity and kinetics.

To assess electrochemical durability, chronoamperometry tests were conducted at a constant potential of −0.20 V for 3600 s. As shown in Fig. 4f, Co-CuS_{ED} exhibited excellent stability under both saturated oxygen and air conditions. To achieve the specific H_2O_2 production, an H-cell was used to collect electrosynthesized H_2O_2 during the chronoamperometry tests. As shown in Fig. 4h, Co-CuS_{ED} achieved a maximum H_2O_2 yield of 1.10 mol g_{cat}^{-1} h^{-1} at −0.20 V (*vs.* RHE) under a saturated O_2 atmosphere, and 1.02 mol g_{cat}^{-1} h^{-1} under air conditions. FE calculated using eqn (S7) was calculated to be 65%, in close agreement with the result using RRDE measurement (Fig. 4b). Compared to recently reported metal sulfides and other catalysts, Co-CuS_{ED} exhibits an exceptional H_2O_2 yield, outperforming most metal sulfide-based catalysts and other kinds of catalysts documented in the current literature (Table S3). To

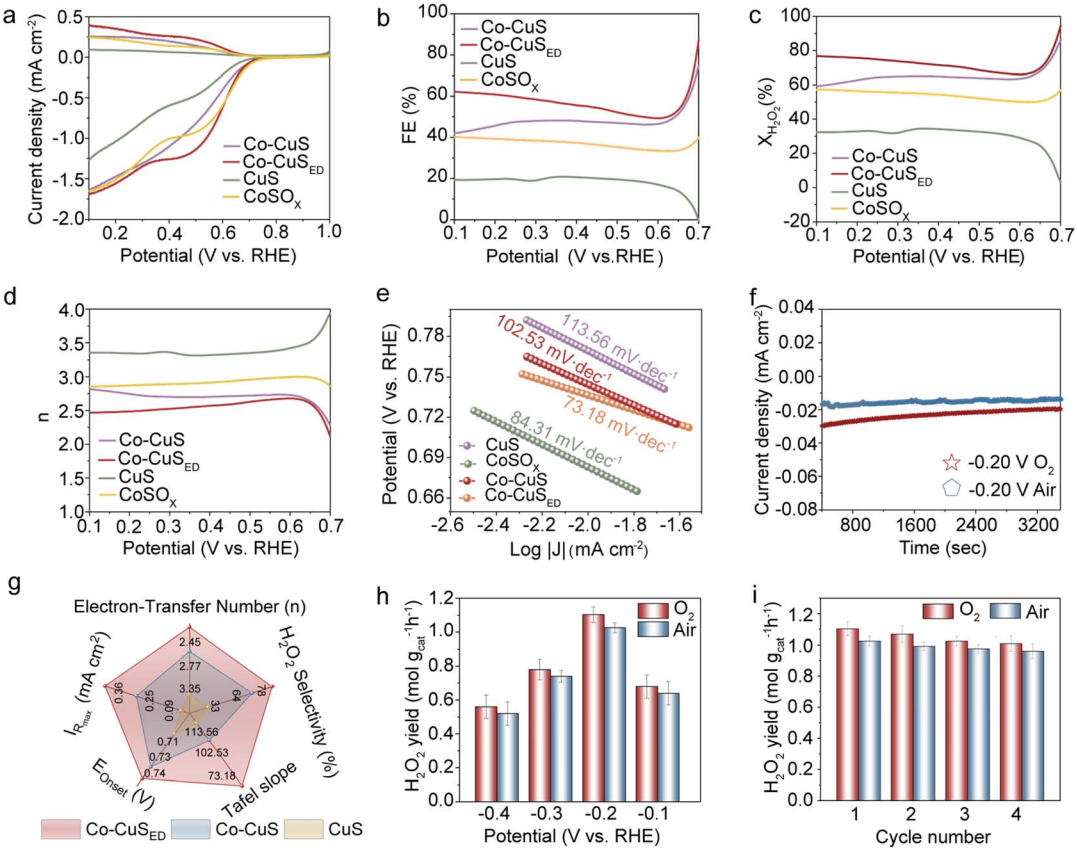

Fig. 4 (a) ORR polarization curves of CuS, Co-CuS, Co-CuS_{ED}, and $CoSO_x$; corresponding FE (b), H_2O_2 selectivity (c) and *n* values (d) at a wide potential window derived from (a). (e) Tafel plots derived from the polarization curves of the disc in (a); (f) chronoamperometric test of Co-CuS_{ED} in both O_2-saturated and air-saturated solution; (g) the Radar chart illustrates the comparative $2e^-$ ORR performance across five parameters of CuS, Co-CuS, and Co-CuS_{ED}; (h) H_2O_2 yield rate *versus* potential under both O_2- and air-saturated conditions; (i) H_2O_2 yield rate *versus* cycle number under both O_2- and air-saturated conditions.

further evaluate the recyclability of H_2O_2 production, cycling tests were conducted under both O_2- and air-saturated conditions. After the 4th cycle, Co-CuS_{ED} maintained a production rate of 1.01 mol g_{cat}^{-1} h^{-1} under O_2 and 0.96 mol g_{cat}^{-1} h^{-1} under air conditions (Fig. 4i), demonstrating excellent reusability of the Co-CuS_{ED} catalyst. Structural characterization was conducted to assess the stability of Co-CuS_{ED} after a four-cycle H_2O_2 electrosynthesis test. As shown in Fig. S13, the XRD pattern retains the original crystal structure of CuS. Furthermore, high-resolution XPS spectra of S 2p, Cu 2p and Co 2p demonstrate the presence of Co dopants after electrochemical cycling. The valence states of all three elements remained unchanged, although peak intensities were slightly reduced compared to the pristine catalyst (Fig. 2d–f)—likely due to partial coverage by the binder used to immobilize the catalyst. Collectively, these results confirm that Co-CuS_{ED} maintains both crystalline framework integrity and surface chemical state stability under repeated electrochemical cycling, highlighting its structural robustness for practical applications. The electrochemical active surface area (ECSA) was determined based on the double-layer capacitance (C_{dl}) in a non-pseudocapacitive potential window since the ECSA is proportional to the C_{dl}. As shown in Fig. S14–S16, Co-CuS_{ED} exhibited a significantly larger C_{dl} compared to CuS and Co-CuS, providing more active sites and substantially enhancing its catalytic performance.

With regards to the excellent electrosynthesis performance of the Co-CuS_{ED}, a dual cathode configuration was adopted to investigate the degradation efficiency of RhB (Fig. 5a), in which working electrode 1 (WE1) was applied to *in situ* generate H_2O_2, while working electrode 2 (WE2) facilitates the decomposition of H_2O_2 into *OH, which are capable of effectively degrading organic dyes. Corresponding photographs of the RhB solution revealed a rapid color change from deep purple to near colorless when using Co-CuS_{ED} as the catalyst. Specifically, the Co-CuS_{ED} configuration achieved near-complete RhB removal, as quantified by the standard calibration curve (Fig. S17), and retained 85% degradation efficiency after three consecutive cycles (Fig. 5b)—significantly outperforming Co-CuS, which exhibited only 53% efficiency under the same conditions (Fig. S18). The optimal potential at WE2 was determined to be −0.20 V; higher potential resulted in reduced RhB degradation efficiency (Fig. S19). To verify whether the RhB degradation is primarily attributed to the *in situ* generated *OH, control experiments were conducted. As shown in Fig. 5c, while RhB was efficiently degraded under standard conditions, the addition of *tert*-

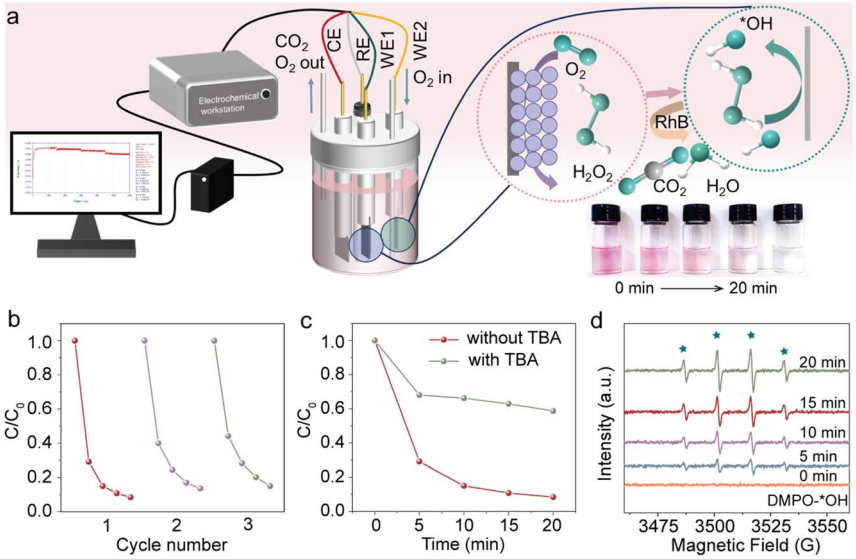

Fig. 5 (a) Schematic illustration of a dual cathode configuration for the degradation of RhB. (b) RhB degradation comparison rate *versus* cycle number using Co-CuS_{ED} as the catalyst. (c) RhB degradation efficiency with/without *tert*-butanol (TBA). (d) EPR spin trapping with dimethyl pyridine *N*-oxide (DMPO) at 0, 5, 10, 15, and 20th minute operation using Co-CuS_{ED} as the catalyst.

butylalcohol (TBA) to the electrolyte significantly reduced degradation efficiency due to its suppression of *OH radical formation,[45] confirming that *OH is the primary oxidant in the system. The *ex situ* electron paramagnetic resonance (EPR) spectrum by using DMPO as the capture agent was obtained to determine the existence of *OH during the electrochemical process. As shown in Fig. 5d, with the increase of reaction times, *OH would be accumulated which would bind with DMPO to form DMPO–*OH adducts, which can be detected by EPR. With the increase of operation time, the signal gradually strengthened, indicating continuous generation of H_2O_2 from the Co-CuS_{ED} cathode and simultaneous conversion of H_2O_2 into *OH *via* WE2. Therefore, Co-CuS_{ED} is favorable for practical RhB degradation due to the excellent *in situ* electrochemical synthesis of H_2O_2 and high working stability.

Conclusions

In summary, Co-CuS_{ED} with optimized interspaced Co dopants and edge defects was successfully designed and constructed for electrocatalytic H_2O_2 synthesis. The hexagonal lamellar arrangement of microspheres provides ample electrochemical interfaces, while the introduction of edge defects and Co dopants enhances the electronic structure of active sites, significantly promoting the $2e^-$-ORR over the $4e^-$-ORR. The volume of H_2O_2 used during synthesis plays a critical role in regulating the concentration of surface Co dopants and edge defects. Consequently, the Co-CuS_{ED} with an optimized 1.0 mL of H_2O_2 demonstrated superior $2e^-$-ORR performance, with yield rate of 1.04 mol g_{cat}^{-1} h^{-1}, along with enhanced faradaic efficiency and H_2O_2 selectivity of 60% and 78%, respectively. In practical applications, a dual cathode configuration using the optimized Co-CuS_{ED} for *in situ* H_2O_2 generation achieved a rapid degradation rate of organic dyes, reaching 92% degradation efficiency within 20 minutes. This research offers a green, low-cost, and efficient strategy for H_2O_2 production and advances the understanding of catalyst design for electrosynthesis, with promising applications in wastewater treatment.

Author contributions

C. S. performed the synthesis, and physical and electrochemical characterization. C. S., J. W. and L. G. conceived and designed the experiments. C. S. wrote the manuscript with assistance from J. W., C. M., Y. M., and Q. Y. All authors participated in the analysis of the data. All authors have given approval to the final version of the manuscript.

Conflicts of interest

There are no conflicts to declare.

Data availability

Supplementary information: experimental section, additional adsorption models, XPS, XRD, SEM, EPR, and electrochemical data, *etc*. See DOI: **https://doi.org/10.1039/d5sc06179b**.

Acknowledgements

This work was financially supported by the National Natural Science Foundation of China (22202114), Natural Science Foundation of Shandong Province (No. ZR2022QB028, ZR2025MS141, and ZR2022MB124), the China Postdoctoral Science Foundation (2021M701694), and Postdoctoral Science Foundation of Jiangsu Province (1006-YBA21038). V. N. and X. G. wish to acknowledge the support of the SFI-funded AMBER Research Centre and the SFI Frontiers for the Future award

(Grant No. 12/RC/2278_P2 and 20/FFP-A/8950 respectively). Furthermore, V. N. and X. G. wish to thank the Advanced Microscopy Laboratory in CRANN for provision of their facilities. The Central Laboratory of Qingdao Agriculture University is also acknowledged for help with physical characterization.

References

1 S. Baccour, G. Goelema, T. Kahil, J. Albiac, M. T. H. Van Vliet, X. Zhu and M. Strokal, Water Quality Management Could Halve Future Water Scarcity Cost-Effectively in the Pearl River Basin, *Nat. Commun.*, 2024, **15**, 5669.

2 Y. Liu, L. Wang, Q. Ma, X. Xu, X. Gao, H. Zhu, T. Feng, X. Dou, M. Eguchi, Y. Yamauchi and X. Yuan, Simultaneous Generation of Residue-Free Reactive Oxygen Species and Bacteria Capture for Efficient Electrochemical Water Disinfection, *Nat. Commun.*, 2024, **15**, 10175.

3 Y. Bi, Near-Infrared H_2O_2 Production via Dual Pathways of O_2 Reduction and H_2O Oxidation, *Sci. China Chem.*, 2023, **66**, 1239–1240.

4 Z. Bao, W. Fang, J. Li, Y. Shao, Y. Li, S. Zhang, X. Peng, C. Jiang, X. Zhong and J. Wang, $Ni_3V_2O_8$ Nanospheres for Sustained and Efficient Enhancement of Electrocatalytic H_2O_2 Production in pH-Universal Solutions, *ACS Catal.*, 2024, **14**, 12140–12151.

5 H. Li, Q. Wan, C. Du, J. Zhao, F. Li, Y. Zhang, Y. Zheng, M. Chen, K. H. L. Zhang, J. Huang, G. Fu, S. Lin, X. Huang and H. Xiong, Layered Pd Oxide on PdSn Nanowires for Boosting Direct H_2O_2 Synthesis, *Nat. Commun.*, 2022, **13**, 6072.

6 H. Zhang, N. Li, S. Gao, A. Chen, Q. Qian, Q. Kong, B. Y. Xia and G. Hu, Quenching-Induced Atom-Stepped Bimetallic Sulfide Heterointerface Catalysts for Industrial Hydrogen Generation, *eScience*, 2024, 100311.

7 C. Ponce de León, *In Situ* Anodic Generation of Hydrogen Peroxide, *Nat. Catal.*, 2020, **3**, 96–97.

8 Y. Zhang, C. Zhang, Y. Mei, T. Le, H. Shao, H. Jiang, Y. Feng and J. Hu, NiFe Layered Double Hydroxide as an Efficient Bifunctional Catalyst for Electrosynthesis of Hydrogen Peroxide and Oxygen, *Int. J. Hydrogen Energy*, 2022, **47**, 36831–36842.

9 Q. Yang, C. Sun, L. Sun, H. Liu, L. Su, C. Ma, J. Wang, L. Gong and Z. Yan, Homogeneous Bismuth Dopants Regulate Cerium Oxide Structure to Boost Hydrogen Peroxide Electrosynthesis via Two-Electron Oxygen Reduction, *Inorg. Chem. Front.*, 2025, **12**, 3384–3392.

10 M. Huang, Z. Cui, Z. Li and W. Sheng, Switching the Oxygen Reduction Route on Pt Using S through d–p Hybridization, *ACS Catal.*, 2024, **14**, 2095–2106.

11 H. Huang, M. Sun, S. Li, S. Zhang, Y. Lee, Z. Li, J. Fang, C. Chen, Y.-X. Zhang, Y. Wu, Y. Che, S. Qian, W. Zhu, C. Tang, Z. Zhuang, L. Zhang and Z. Niu, Enhancing H_2O_2 Electrosynthesis at Industrial-Relevant Current in Acidic Media on Diatomic Cobalt Sites, *J. Am. Chem. Soc.*, 2024, **146**, 9434–9443.

12 Y. Wang, Z. Yang, C. Zhang, Y. Feng, H. Shao, J. Chen, J. Hu and L. Zhang, Fabricating Carbon Quantum Dots of Graphitic Carbon Nitride vis Ultrasonic Exfoliation for Highly Efficient H_2O_2 Production, *Ultrason. Sonochem.*, 2023, **99**, 106582.

13 Y. Tian, D. Deng, L. Xu, M. Li, H. Chen, Z. Wu and S. Zhang, Strategies for Sustainable Production of Hydrogen Peroxide via Oxygen Reduction Reaction: From Catalyst Design to Device Setup, *Nano–Micro Lett.*, 2023, **15**, 122.

14 Y. Zhang, M. Wang, W. Zhu, M. Fang, M. Ma, F. Liao, H. Yang, T. Cheng, C. Pao, Y. Chang, Z. Hu, Q. Shao, M. Shao and Z. Kang, Metastable Hexagonal Phase SnO_2 Nanoribbons with Active Edge Sites for Efficient Hydrogen Peroxide Electrosynthesis in Neutral Media, *Angew. Chem.-Int. Ed.*, 2023, **62**, e202218924.

15 X. Zhang, C. Zhang, C. Yu and C. Liu, Metal–Organic Frameworks for Electrocatalytic Hydrogen Peroxide Production, *Mater. Chem. Front.*, 2024, **8**, 1084–1100.

16 Q. Sun, G. Xu, B. Xiong, L. Chen and J. Shi, Anion-Tuned Nickel Chalcogenides Electrocatalysts for Efficient $2e^-$ ORR towards H_2O_2 Production in Acidic Media, *Nano Res.*, 2023, **16**, 4729–4735.

17 R. D. Ross, H. Sheng, Y. Ding, A. N. Janes, D. Feng, J. R. Schmidt, C. U. Segre and S. Jin, Operando Elucidation of Electrocatalytic and Redox Mechanisms on a 2D Metal Organic Framework Catalyst for Efficient Electrosynthesis of Hydrogen Peroxide in Neutral Media, *J. Am. Chem. Soc.*, 2022, **144**, 15845–15854.

18 X. Ren, X. Dong, L. Liu, J. Hao, H. Zhu, A. Liu and G. Wu, Research Progress of Electrocatalysts for the Preparation of H_2O_2 by Electrocatalytic Oxygen Reduction Reaction, *SusMat*, 2023, **3**, 442–470.

19 F. Zhang, Y. Zhu, C. Tang, Y. Chen, B. Qian, Z. Hu, Y. Chang, C. Pao, Q. Lin and S. A. Kazemi, High-efficiency Electrosynthesis of Hydrogen Peroxide from Oxygen Reduction Enabled by a Tungsten Single Atom Catalyst with Unique Terdentate N_1O_2 Coordination, *Adv. Funct. Mater.*, 2022, **32**, 2110224.

20 H. Chen, C. He, H. Niu, C. Xia, F.-M. Li, W. Zhao, F. Song, T. Yao, Y. Chen and Y. Su, Surface Redox Chemistry Regulates the Reaction Microenvironment for Efficient Hydrogen Peroxide Generation, *J. Am. Chem. Soc.*, 2024, **146**, 15356–15365.

21 H. Niu, L. Huang, Y. Qin, R. Qi, B. Mei, D. Wu, F.-M. Li, B. You, Q. Li, Y. Yao, Z. Wang, T. Yao, S. Ding, W. Guo, Y. Chen, Y. Su, F. Song and Y. Xia, Hydrogen Peroxide Spillover on Platinum–Iron Hybrid Electrocatalyst for Stable Oxygen Reduction, *J. Am, Chem, Soc.*, 2024, **146**, 22650–22660.

22 H. Jiang, Y. Wang, J. Hu, X. Shai, C. Zhang, T. Le, L. Zhang and M. Shao, Phase Regulation of WO_3 for Highly Selective Oxygen Reduction to Hydrogen Peroxide, *Chem. Eng. J.*, 2023, **452**, 139449.

23 X. Mei, X. Zhao, Y. Chen, B. Deng, Q. Geng, Y. Cao, Y. Li and F. Dong, Highly Efficient H_2O_2 Production via Two-Electron Electrochemical Oxygen Reduction over Fe-Doped CeO_2, *ACS Sustainable Chem. Eng.*, 2023, **11**, 15609–15619.

24 Z. Yang, Y. Gao, L. Zuo, C. Long, C. Yang and X. Zhang, Tailoring Heteroatoms in Conjugated Microporous

Polymers for Boosting Oxygen Electrochemical Reduction to Hydrogen Peroxide, *ACS Catal.*, 2023, **13**, 4790–4798.

25 D. Deng, W. Zhang, J. Qian, Y. Chen, C. Pu, H. Li, H. Li and L. Xu, Charge Delocalization Regulation of Atomically Dispersed Tungsten Sites by Axial Sulfur Atoms for Highly Active Oxygen Reactions in Low-Temperature Zinc-air Batteries, *Nano Energy*, 2025, **134**, 110579.

26 S. Chen, X. Liu, J. Xiong, L. Mi, X. Z. Song and Y. Li, Defect and Interface Engineering in Metal Sulfide Catalysts for the Electrocatalytic Nitrogen Reduction Reaction: A Review, *J. Mater. Chem. A*, 2022, **10**(13), 6927–6949.

27 M. Wang, C.-L. Dong, Y.-C. Huang and S. Shen, Operando Spectral and Electrochemical Investigation into the Heterophase Stimulated Active Species Transformation in Transition-Metal Sulfides for Efficient Electrocatalytic Oxygen Evolution, *ACS Catal.*, 2020, **10**, 1855–1864.

28 B. Yan, D. Krishnamurthy, C. H. Hendon, S. Deshpande, Y. Surendranath and V. Viswanathan, Surface Restructuring of Nickel Sulfide Generates Optimally Coordinated Active Sites for Oxygen Reduction Catalysis, *Joule*, 2017, **1**, 600–612.

29 Z. Wang, X. Liao, M. Zhou, F. Huang, K. A. Owusu, J. Li, Z. Lin, Q. Sun, X. Hong, C. Sun, Y. Cheng, Y. Zhao and L. Mai, Interfacial and Vacancies Engineering of Copper Nickel Sulfide for Enhanced Oxygen Reduction and Alcohols Oxidation Activity, *Energy Environ. Mater.*, 2023, **6**, e12409.

30 L. Wang, H.-N. Liu, X. Meng, C.-H. Sun, H.-D. Liu, L.-Y. Gong, Z.-H. Yan and J. Wang, Phase Modulation of Nickel-Tin Alloys in Regulating Electrocatalytic Nitrogen Reduction Properties, *Rare Met*, 2024, **43**, 2851–2858.

31 M. S. A. Sher Shah, G. Y. Jang, K. Zhang and J. H. Park, Transition Metal Carbide-based Nanostructures for Electrochemical Hydrogen and Oxygen Evolution Reactions, *EcoEnergy*, 2023, **1**, 344–374.

32 X. Wang, M. Yu and X. Feng, Electronic Structure Regulation of Noble Metal-Free Materials toward Alkaline Oxygen Electrocatalysis, *eScience*, 2023, **3**, 100141.

33 L. Zheng, M. Niu, T. Zeng, X. Ge, Y. Wang, C. X. Guo, W. Yuan, D. Cao, L. Y. Zhang and C. M. Li, Assembling Molybdenum-Doped Platinum Clusters into a Coral-like Nanostructure for Highly Enhanced Oxygen Reduction, *eScience*, 2024, **4**, 100187.

34 Z. Ju, X. Zhang, Y. Wang, Y. Liang, F. Yu and Y. Liu, Study on ORR Reaction of B-Doped Graphene Supported Co Atoms with Different Defects, *Comput. Theor. Chem.*, 2024, **1233**, 114506.

35 T. Zhu, C. Xia, B. Wu, J. Pan, H. Yang, W. Zhang and B. Y. Xia, Inbuilt Photoelectric Field of Heterostructured Cobalt/Iron Oxides Promotes Oxygen Electrocatalysis for High-Energy-Efficiency Zinc-Air Batteries, *Appl. Catal. B: Environ. Energy*, 2024, **357**, 124315.

36 T. Xu, M. Liu, K. Wu and C. Liu, Density Functional Theory Calculations to Increase the Efficiency of Oxygen Electrode Catalysts from Ytterbium Single Atom Catalysts Using Nitrogen Solid Supports, *ACS Appl. Nano Mater.*, 2024, **7**, 15526–15534.

37 S. Siahrostami, A. Verdaguer-Casadevall, M. Karamad, D. Deiana, P. Malacrida, B. Wickman, M. Escudero-Escribano, E. A. Paoli, R. Frydendal, T. W. Hansen, I. Chorkendorff, I. E. L. Stephens and J. Rossmeisl, Enabling Direct H_2O_2 Production through Rational Electrocatalyst Design, *Nat. Mater.*, 2013, **12**, 1137–1143.

38 A. Zhang, Z. Jiang, S. Zhang, P. Lan, N. Miao, W. Chen, N. Huang, X. Tian, Y. Liu and Z. Cai, Coral-Shaped Mn-CuS with Hierarchical Pores and Crystalline Defects for High-Efficiency H_2O_2 Production via Electrocatalytic Two-Electron Reduction, *Appl. Catal., B*, 2023, **331**, 122721.

39 L. Tabassum, M. Khairul Islam, I. P. Perera, M. Li, X. Huang, H. Tasnim and S. L. Suib, Facile Synthesis of Transition-Metal-Doped (Fe, Co, and Ni) CuS/CuO/CS Nanorod Arrays for Superior Electrocatalytic Oxygen Evolution Reaction, *ACS Appl. Energy Mater.*, 2022, **5**, 12039–12048.

40 X. Wei, Z. Li, H. Jang, M. Gyu Kim, S. Liu, J. Cho, X. Liu and Q. Qin, Switching Product Selectivity in CO_2 Electroreduction via Cu− S Bond Length Variation, *Angew. Chem.-Int. Ed.*, 2024, **63**, e202409206.

41 P. F. Lindberg, S. M. Gorantla, A. E. Gunnæs, B. G. Svensson and E. V. Monakhov, Electronic Properties and Morphology of Copper Oxide/n-Type Silicon Heterostructures, *J. Phys.: Condens. Matter*, 2017, **29**, 315701.

42 H. Liu, S. Zhang, Y. Chai and B. Dong, Ligand Modulation of Active Sites to Promote Cobalt-Doped 1T-MoS_2 Electrocatalytic Hydrogen Evolution in Alkaline Media, *Angew. Chem.-Int. Ed.*, 2023, **62**, e202313845.

43 C. F. Wen, M. Zhou, P. F. Liu, Y. Liu, X. Wu, F. Mao, S. Dai, B. Xu, X. L. Wang, Z. Jiang, P. Hu, S. Yang, H. F. Wang and H. G. Yang, Highly Ethylene-Selective Electrocatalytic CO_2 Reduction Enabled by Isolated Cu−S Motifs in Metal–Organic Framework Based Precatalysts, *Angew. Chem.-Int. Ed.*, 2022, **61**, e202111700.

44 Y. Cao, Y. Zhu, C. Du, X. Yang, T. Xia, X. Ma and C. Cao, Anionic Te-Substitution Boosting the Reversible Redox in CuS Nanosheet Cathodes for Magnesium Storage, *ACS Nano*, 2022, **16**, 1578–1588.

45 Z. Gao, D. Zhang and Y.-S. Jun, Does Tert-Butyl Alcohol Really Terminate the Oxidative Activity of $^{\bullet}OH$ in Inorganic Redox Chemistry?, *Environ. Sci. Technol.*, 2021, **55**(15), 10442–10450.